

# A 1.0 Mbps 198 pJ/bit Bluetooth Low Energy (BLE) Compatible Single Sideband Backscatter Uplink for the NeuroDisc Brain-Computer Interface

James Rosenthal, *Student Member, IEEE*, and Matthew S. Reynolds, *Senior Member, IEEE*

**Abstract**—Wireless brain-computer interfaces (BCIs) are highly energy constrained due to the need to minimize battery size and weight, as well as the need to minimize thermal dissipation into living tissue. We demonstrate an ultra-low power Bluetooth Low Energy (BLE) v5.0 compatible backscatter communication uplink for the NeuroDisc BCI. This backscatter approach is compatible with completely unmodified BLE devices such as PCs, smartphones and tablets, and has an energy consumption of under 200 pJ/bit, over 50X less than commercially-available BLE transmitters. This work is the first to present an analysis and demonstration of single sideband (SSB) BLE backscatter, which increases available channel power by +3 dB while suppressing out-of-channel emissions. An analytic model of SSB backscatter communication is provided, along with simulations showing how non-idealities in the achieved backscatter constellation impact opposite-sideband suppression. Experimental measurements of in-channel gain and opposite-sideband suppression are provided. Additional experiments demonstrate a range of 6 meters using a +20 dBm external carrier source and an unmodified Nordic Semiconductor nRF51DK BLE adapter, while uplinking pre-recorded neural data sampled at 500 Hz.

**Index Terms**—backscatter communication, full-duplex radios, RFID, brain computer interfaces, biomedical devices, neural recording

## I. INTRODUCTION

WIRELESS BRAIN-COMPUTER interfaces (BCIs) enable neuroscientists to investigate the relationship between neural activity and high-level behaviors [1]. However, freely moving experiments are generally limited to 1-2 days due to the limited battery life of wireless neural recording devices [2]. Developing energy-efficient wireless BCIs that easily integrate into existing wireless infrastructure could improve the quality of wireless neurophysiological experiments.

Ideally, researchers could collect neural data over multiple days or weeks in freely moving animals, capturing the broad temporal characteristics of neural dynamics. Performing these experiments in freely moving animals would improve data quality by reducing measurement stereotyping caused by constrained environments [3]. However, a critical obstacle towards this goal has been the severe size, weight, and power constraints on wireless neural recording devices. As a result,

Manuscript received March 11, 2019; revised MONTH XX, 2019; accepted MONTH XX, 2019. Date of publication MONTH, 2019.

This paper is an expanded version from the IEEE MTT-S Radio and Wireless Week (WiSNET), Orlando, FL, USA, January 20-23, 2019.

Corresponding authors: J. Rosenthal (e-mail: jamesrosenthal@gmail.com) J. Rosenthal and M. S. Reynolds are with the Department of Electrical & Computer Engineering, University of Washington, Seattle, WA 98195, USA.

This material is based upon work supported by the National Science Foundation Graduate Research Fellowship under Grant No. DE-1762114.

Color versions of one or more of the figures in this letter are available online at <http://ieeexplore.ieee.org>.

Digital Object Identifier 10.1109/TMTT.2019.0000000

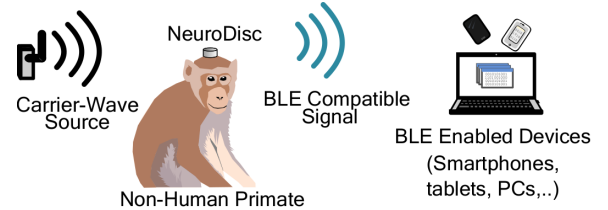


Fig. 1. Conceptual sketch of the NeuroDisc BLE-compatible backscatter data uplink approach

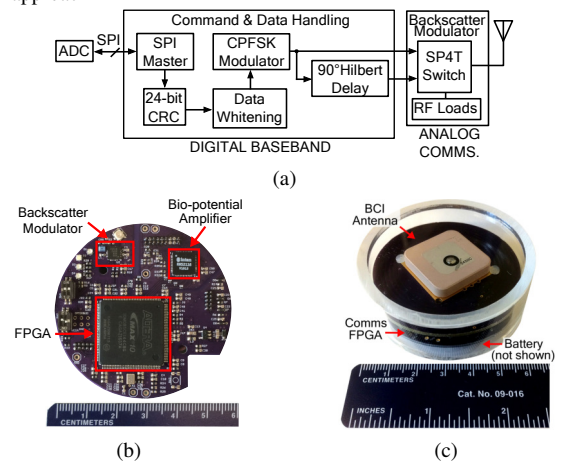


Fig. 2. NeuroDisc hardware architecture: (a) Block diagram of FPGA digital logic (b) Photo of Comms FPGA board (c) Photo of the complete NeuroDisc package

existing wireless neural recording systems cannot continuously stream multiple channels of broadband neural data for more than 1-2 days.

A major reason for the short recording durations of neural sensors is that conventional wireless uplinks consume a disproportionate amount of the energy budget. Wireless neural sensors using commercially-available Bluetooth Low Energy (BLE) chips expend approximately 10 nJ/bit [4]–[6]. WiFi chipsets similarly consume  $\approx 4$  nJ/bit. Fully-custom ultra-wideband active radios have achieved efficiencies below 200 pJ/bit [2], but these systems are not compatible with commonly available off-the-shelf wireless systems.

One method for improving the energy efficiency of wireless neural uplinks is to use backscatter communication, and uplink data by modulating the reflected amplitude, frequency, and/or phase of a carrier wave provided by an external emitter. Backscatter greatly reduces the uplink energy burden for energy-poor devices such as neural interfaces, because the power-hungry functions of carrier-wave generation and radio-frequency (RF) amplification are re-partitioned to an energy-rich external system. However, a key trade-off with backscatter

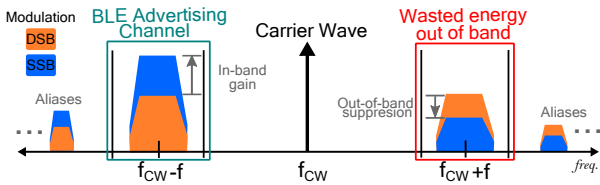


Fig. 3. SSB backscatter modulation can improve the reflected power of the desired sideband image

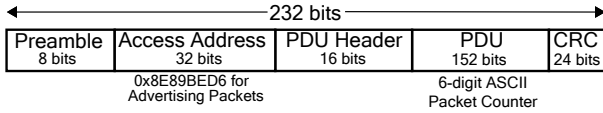


Fig. 4. Overview of the BLE advertising packet structure with the custom packet counter

communication is a less favorable link budget compared to conventional radios, because the carrier must make a round-trip via the backscatter device [7]. As a result, backscatter devices often require complex custom receivers to extract the relatively low-power backscatter signal.

To reduce the burden of custom receivers, recent research has sought to integrate backscatter communications with existing wireless infrastructure. BLE compatible backscatter communications were developed in [4] to send static advertising packets to commodity BLE receivers (e.g. smartphones, tablets, computers) and to send dynamic sensor data in [8]. In [9], a system was developed that could backscatter IEEE 802.11 WiFi- or IEEE 802.15.4 Zigbee-compliant packets, and LoRA compatible packets in [10]. Additional research has explored ways to improve spectral efficiency of backscatter modulation. Pulse-shaping was explored in [11], however, that work still requires the use of energy-hungry analog biasing circuitry. Single sideband (SSB) backscatter modulation was demonstrated for WiFi and Zigbee packets in [9], however, an analysis of the theoretical vs. realizable performance of SSB backscatter was not presented in that work.

In this work, we present the first analysis and demonstration of SSB BLE-compatible backscatter communication with a per-bit energy consumption 50X lower than commercial off-the-shelf BLE transmitters. The system was implemented on the NeuroDisc BCI [12] (Fig. 2) and expands on previous work in [8] that presented double sideband (DSB) BLE backscatter for wirelessly streaming sensor data. SSB modulation improves spectral efficiency [13]–[15] and reduces out-of-band emissions for regulatory compliance, for example, as specified by the U.S. Federal Communications Commission (FCC) (Fig. 3). This paper adds to the state-of-the-art by providing a theoretical framework for SSB backscatter communication and an analysis of the effects of quadrature skew on sideband suppression resulting from imperfect reflection coefficients.

## II. NEURODISC SYSTEM OVERVIEW

The NeuroDisc comprises a multi-channel ADC to acquire sensor data, an Altera MAX10 FPGA, and a backscatter modulator to uplink data (Fig. 2). An Intan RHS2116 analog front-end is used for the bio-potential amplifier, and it provides a

TABLE I  
MEASURED NEURODISC POWER BUDGET

	Current (mA)	Power (mW)	% of total
<b>Intan RHS2116 IC</b>	3.27	10.8	5.63 %
<b>FPGA (static baseline)</b>	53.11	175.3	91.35 %
<b>FPGA (dynamic)</b>	1.69	5.59	2.91 %
<b>Backscatter Modulator</b>	0.060	0.198	0.10 %
<b>Total (static+dynamic)</b>	58.13	191.89	

16-channel, 16-bit resolution data acquisition system intended for bio-sensing applications [16]. Power is provided to the NeuroDisc by a single-cell 500 mAh lithium polymer battery. The power budget for the NeuroDisc is provided in Table I.

The Altera MAX10 FPGA performs command and data handling for the NeuroDisc. It controls the multi-channel ADC via SPI to sample and digitize sensor data. BLE advertising packets are then formed by computing a 24-bit CRC and applying data whitening (Fig. 2(a) and (4)). These packets are modulated using continuous-phase frequency-shift keying (CPFSK) and serially output to the backscatter modulator of Fig. 5(a). The backscatter modulator is implemented with an Analog Devices ADG904 SP4T CMOS RF switch. Four distinct impedances are connected to the RF switch, and are chosen as described in Section III-E below.

## III. SSB BLE SPECTRUM DESIGN APPROACH & RESULTS

### A. Bluetooth Low Energy (BLE) Overview

The Bluetooth Core Specification v5.0 [17] defines the physical- and link-layer requirements for BLE-compatible advertising messages. BLE systems are required to operate in 2.4 GHz ISM band at 2.400–2.4835 GHz. The band allocates three channels that are 2 MHz wide for uni-directional advertising: CH37 at 2.402 GHz, CH38 at 2.426 GHz, and CH39 at 2.481 GHz. The BLE advertising packets have a configurable length between 80 and 376 bits. Each packet is composed of five required fields: a preamble, an Access Address (defined to be 0x8E89BED6 for advertising packets), a Protocol Data Unit (PDU) header, a PDU containing data, and a 24-bit CRC calculated using the previous fields. After the packet is constructed, a data whitening filter is applied.

For the NeuroDisc, all packets are generated in the FPGA. The PDU length is set to 152 bits to incorporate a 16-bit ADC sample and a 6-bit packet counter to detect dropped packets. These data are transmitted as ASCII symbols to render them easily readable on commodity BLE scanners (e.g. smartphones). All other fields are constructed per the BLE specification, resulting in a packet length of 232 bits.

### B. BLE Modulation Parameters

BLE requires that a device modulate data using binary frequency-shift keying at a symbol rate of 1.0 Msymbols/s. Data bits are encoded in the frequency deviation relative to channel's center frequency. A '1' is represented by a positive frequency shift and a '0' is represented by a negative frequency shift.

The subcarrier frequencies for BLE backscatter can be chosen by considering the BLE signal-to-interference ratio

(SIR) requirement and the backscatter modulator's power consumption. SIR is the ratio of the BLE signal's power to the power of an undesired interfering signal. If the SIR is lower than the requirement (i.e. if the interference signal is too strong relative to the BLE signal), then the receiver may drop packets. A key trade-off is that as the external carrier-wave (CW) frequency is moved further from the advertising channel center frequency, it can emit at a higher power to achieve a farther range with less interference; however, the subcarrier modulating frequencies must be higher, which increases the power consumption of the backscatter modulator. The BLE specification requires that the receiver maintain a BER  $\leq 0.1\%$  for a minimum SIR of  $-27$  dB for adjacent interference  $\geq 3$  MHz from a channel's center frequency. A systematic test of CW induced blocking of a BLE receiver was documented in [18]. In general, the trade-offs in power consumption and SIR will be dependent on the specific backscatter modulator, BLE receiver, and oscillators used in the design. Important considerations are the power consumption of the RF switch as a function of switching rate, the ON/OFF switching time of the RF switch which could limit the maximum switching frequency, and the actual packet error rate vs. SIR performance of the specific BLE receiver used.

### C. Transmitting BLE Advertising Packets via Backscatter

BLE-compatible backscatter signals can be created via simultaneous phase-shift keying (PSK) and continuous phase frequency-shift keying (CPFSK) modulation processes. Frequency-shift keying communication systems often use a CPFSK modulation process to reduce undesired spectral sidelobes [14], [15]. In traditional active radio architectures, CPFSK is used to modulate a carrier wave, however, since a backscatter device does not generate its own carrier signal, CPFSK is instead used to actuate a PSK modulator that will in turn modulate an externally generated carrier incident upon the backscatter device. The PSK process occurs at the backscatter modulator by reflecting the incident carrier wave using switched impedances, while the CPFSK process is generated numerically inside the FPGA to create a digital CPFSK control signal modulated by baseband data from the advertising packet. The CPFSK control signal actuates the RF switch of the backscatter modulator, which connects the antenna to one of the RF loads shown in Fig. 5 and thus changes the reflection coefficient of the antenna. To transmit a '1', the FPGA generates a CPFSK control signal at subcarrier frequency  $f_{sc1}$ , and to transmit a '0', it modulates the signal at subcarrier frequency  $f_{sc0}$ . Thus the reflection coefficient at the antenna will change as the CPFSK signal actuates the RF switch, resulting in PSK modulation of the incident CW.

### D. DSB Backscatter Modulation

To perform DSB backscatter modulation, we use a CPFSK control signal to actuate an RF switch. The CPFSK control signal,  $s(t)$ , is a square wave whose frequency changes based on the current symbol,  $b_n \in \{0, 1\}$ , and whose phase varies based on the current and past symbols (i.e.  $s$  has memory).

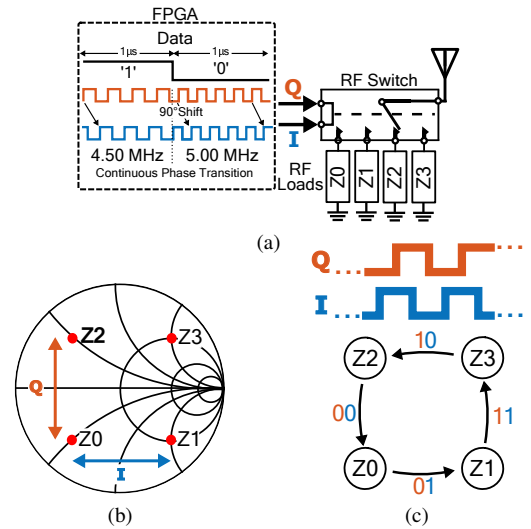


Fig. 5. Implementation overview: (a) Method for SSB backscatter using in-phase (I) and quadrature (Q) control signals, (b) Smith chart view of the ideal reflection states, (c) State-machine depiction of the SSB modulation process

Over a single BLE data bit period, the CPFSK control signal can be expressed as

$$s(t) = \Pi\left(2\pi ft + \frac{\pi(-1)^{b_{n+1}}}{2T_b}(t - nT_b) + \phi_n\right), \quad nT_b < t \leq (n+1)T_b \quad (1)$$

where  $\Pi(\cdot)$  is a square wave signal, the center frequency  $f$  is  $f = \frac{f_{sc0} + f_{sc1}}{2}$ ,  $\frac{\pi}{2T_b}(-1)^{b_{n+1}}$  is the phase modulation term dependent on the current symbol,  $n$  is the bit number,  $T_b$  is the bit period (1.0  $\mu$ sec for BLE), and  $\phi_n$  is a residual phase term. For the phase of  $s(t)$  to be continuous between symbols,  $\phi_{n+1} = \frac{\pi}{2}(-1)^{b_{n+1}} + \phi_n$ .

As the control signal switches states, the antenna is switched between different discrete loads, thus changing its reflection coefficient. For DSB modulation, two complex-valued reflection states are used:

$$\Gamma_{dsb}(s(t)) = \begin{cases} \Gamma_0 = A_0 e^{j\phi_0}, & s(t) = 0 \\ \Gamma_1 = A_1 e^{j\phi_1}, & s(t) = 1 \end{cases} \quad (2)$$

with  $|A_{0,1}| \leq 1$ ,  $\phi_{0,1} = [0, 2\pi)$ , and  $\Gamma_1 \neq \Gamma_0$ .

The modulated signal reflected from the NeuroDisc can be determined by the definition of the reflection coefficient [19]

$$V^-(t) = \Gamma_{dsb}(s(t)) \cdot V^+(t), \quad (3)$$

where  $V^-$  is the reflected signal and  $V^+$  is the incident CW signal. If we consider  $V^+(t)$  as a single-tone sinusoidal CW, the reflected DSB signal becomes

$$V^-(t) = \Gamma_{dsb}(s(t)) \cdot \cos(2\pi f_{cw}t) \quad (4)$$

While the backscatter modulation described above can generate BLE-compatible signals, energy is wasted by generating USB and LSB images of equal magnitude about the carrier frequency, even though the receiver passband includes only one of the images [20]. This undesired sideband could also interfere with other nearby communication systems and violate RF emissions regulations. One way to recover the lost energy and reduce unwanted emissions is by implementing SSB modulation.

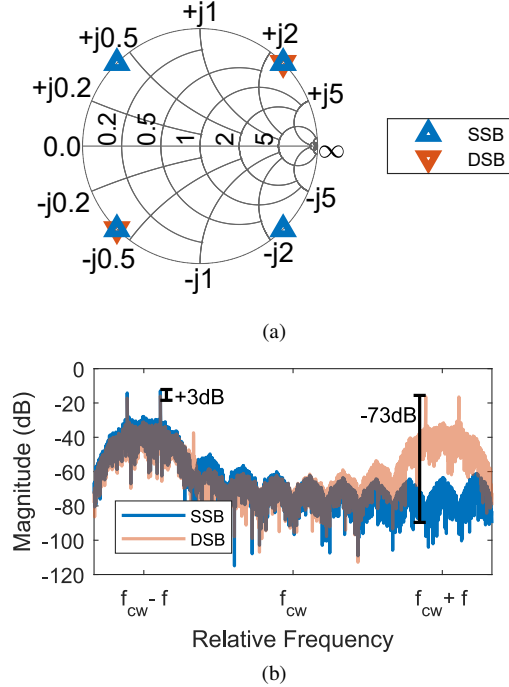


Fig. 6. Simulation of SSB and DSB modulation using an ideal constellation, (a) Smith chart plot of the impedance constellation, (b) Simulated power spectral densities between SSB and DSB backscatter modulation

### E. SSB Backscatter Modulation

In DSB modulation, the message signal is fully encoded in both of the sidebands, so recovering either the upper- or lower-sideband image is sufficient for decoding the message. SSB modulation enables more efficient use of bandwidth and power by encoding the message into just one of the sidebands, as shown in Fig. 3.

One method for achieving SSB modulation is to use the phasing method [13]. The SSB signal  $x_{ssb}(t)$  can be seen as a special case of quadrature amplitude modulation, and it can be written as

$$x_{ssb}(t) = x(t) \cdot \cos(2\pi f_c t) \pm \hat{x}(t) \cdot \sin(2\pi f_c t), \quad (5)$$

where  $x(t)$  is the message signal,  $\hat{x}(t)$  is its Hilbert transform [15],  $f_c$  is the carrier frequency, and the plus-or-minus determines which sideband is retained. The Hilbert transform can be seen as a linear filter that shifts the phase on an incoming signal by  $-90^\circ$  across all frequencies (i.e. a time delay of a quarter-period when the input function is a baseband square-wave signal).

In the case of SSB BLE backscatter modulation, the backscattered signal is a function of the instantaneous reflection coefficient, so we can express the reflected SSB signal  $V_{ssb}^-(t)$  as

$$V_{ssb}^-(t) = \Gamma_{ssb}(s(t), \hat{s}(t)) \cdot \cos(2\pi f_{cw} t) \quad (6)$$

where  $f_{cw}$  is the frequency of the externally-supplied CW.

Equation (6) can be shown to match the form of (5) by implementing time-dependent, complex-valued reflection coefficients. The reflection coefficient  $\Gamma_{ssb}(t)$  can be designed such that its real and imaginary parts are determined by the CPFSK modulator control signal,  $s(t)$ , and its Hilbert

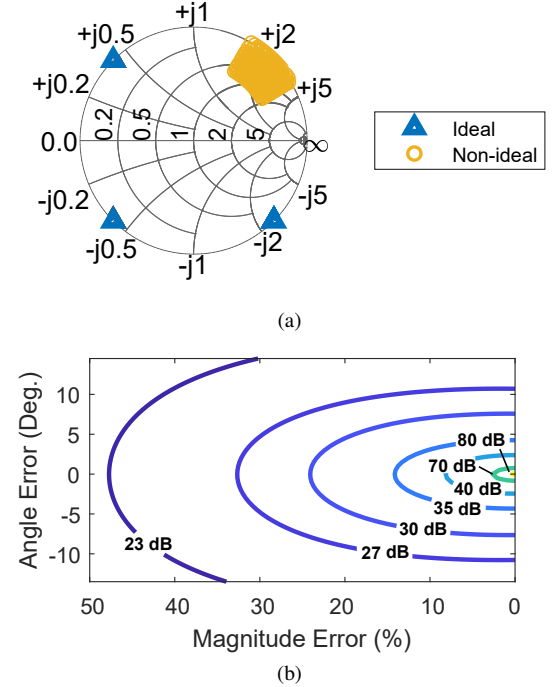


Fig. 7. Simulation of SSB modulation using non-ideal constellation points. (a) Smith chart plot of the non-ideal constellation, (b) Contour plot of the SSB suppression ratio for one constellation point with magnitude and phase angle error. Reduced SSB suppression would be achieved for magnitude and phase errors in multiple constellation points.

transform  $\hat{s}(t)$ , respectively. Consider four complex reflection coefficients:

$$\Gamma_{ssb}(s(t)) = \begin{cases} \Gamma_0 = A_0 e^{j\phi_0}, & s(t) = 0, \hat{s}(t) = 0 \\ \Gamma_1 = A_1 e^{j\phi_1}, & s(t) = 0, \hat{s}(t) = 1 \\ \Gamma_2 = A_2 e^{j\phi_2}, & s(t) = 1, \hat{s}(t) = 0 \\ \Gamma_3 = A_3 e^{j\phi_3}, & s(t) = 1, \hat{s}(t) = 1 \end{cases} \quad (7)$$

with  $|\Gamma_0| = |\Gamma_1| = |\Gamma_2| = |\Gamma_3|$  and the angles of the four states are as shown in the ideal constellation of Fig. 5(b). If we split the reflection coefficients of (7) into their real and imaginary parts such that  $Ae^{j\phi} = \Gamma_I + j\Gamma_Q$ , then we can express (6) as

$$\begin{aligned} V_{ssb}^-(t) &= [\Gamma_I(s(t)) + j\Gamma_Q(\hat{s}(t))] \cdot \cos(2\pi f_{cw} t) \\ &= \Gamma_I(s(t)) \cdot \cos(2\pi f_{cw} t) - \\ &\quad \Gamma_Q(\hat{s}(t)) \cdot \sin(2\pi f_{cw} t) \end{aligned} \quad (8)$$

where  $\Gamma_i = \Gamma_I + j\Gamma_Q$  for  $i \in \{0, 1, 2, 3\}$ . To suppress the other sideband image, the subtraction in Eq. (8) can be changed to addition.

### F. Simulation of SSB Backscatter Modulation

Simulations in MATLAB evaluated the performance of SSB backscatter modulation. The simulations had two goals: to validate whether SSB backscatter modulation would offer improved spectral performance compared to DSB backscatter, and to analyze how a non-ideal impedance constellation (i.e. quadrature skew) would affect opposite-sideband suppression. The simulations compared the power spectral densities generated by SSB and DSB backscatter modulation. The power

spectral densities were computed for the transmission of one BLE advertising packet using DSB and SSB backscatter modulation as described in (4) and (6), respectively. The ideal constellation shown in Fig. 6(a) was used. A comparison of the power spectral densities for each modulation scheme revealed that ideal SSB modulation yielded a 3 dB increase in power for the desired sideband image and >70 dB of sideband suppression for the undesired sideband image (Fig. 6). These simulation results match expectations that the power from the suppressed sideband would be constructively added to the desired sideband, doubling its in-band power. The opposite-sideband suppression ratio would ideally be infinite, however, the simulated result matches our intuition given numeric rounding errors.

The SSB simulations were repeated with non-ideal constellations to analyze how sideband suppression changed with component variations. One disadvantage of SSB backscatter modulation is that opposite-sideband suppression is limited by quadrature skew. Quadrature skew results from magnitude and phase errors in the realized impedance constellation. For the simulations, the magnitude and phase angle of one symbol in the constellation were altered by up to 50% magnitude and  $\pm 15^\circ$  phase relative to the ideal values (Fig. 7(a)). For each deviation, the SSB suppression ratio was calculated as the ratio of the power in the lower sideband image (i.e. the desired sideband) to the power in the upper sideband image (i.e. the undesired sideband). From the results shown in Fig. 7(b) we see that small deviations significantly degrade the SSB suppression ratio, e.g. 0.5% error in magnitude or phase reduces SSB suppression by nearly 20 dB. Such deviations could arise due to variations in component values. For example, the calculated value of an inductor for symbol impedance Z3 at 2.4 GHz yields a value of 7.95 nH. Given an impedance tolerance of  $\pm 10\%$ , the resulting symbol impedance could have a phase error of  $+5^\circ/-3^\circ$ , which would reduce SSB suppression to approximately 35 dB. Further, additional performance degradation would be witnessed if additional symbol impedances had magnitude and/or phase angle errors. These results emphasize the importance of precise component values and careful circuit layout to achieve optimal performance.

#### IV. LINK BUDGET

The free-space link budget for the NeuroDisc was derived following the approaches of [21] and [22]. We considered a bistatic dislocated configuration, because the NeuroDisc, the CW source, and BLE receiver are separate entities, as shown in Fig. 1. All antennas are assumed to be optimally aligned and matched. The backscattered power from the NeuroDisc,  $P_{\text{ND}}$ , can be calculated as

$$P_{\text{ND}} = \frac{P_{\text{T}}G_{\text{T}}\Delta\sigma}{4\pi r_{\text{t}}^2}, \quad (9)$$

where  $P_{\text{T}}$  is the power transmitted from the CW source,  $G_{\text{T}}$  is the gain of the CW source antenna,  $r_{\text{t}}$  is the distance between the CW source and the NeuroDisc antenna, and  $\Delta\sigma$  is the differential radar cross-section (RCS) of the NeuroDisc. In [7], analytic expressions are provided to calculate the

TABLE II  
LINK BUDGET PARAMETERS USED FOR THE EXPERIMENTAL VALIDATION

$P_{\text{T}}$	$G_{\text{ND}}$	$G_{\text{T}}$	$G_{\text{R}}$	$\lambda$
0.1 W (20 dBm)	2.2 dBi	2.2 dBi	2.2 dBi	0.1246 m
$Z_{\text{a}}$	$Z_{\text{0}}$	$Z_{\text{1}}$	$Z_{\text{2}}$	$Z_{\text{3}}$
$50 + j 0 \Omega$	$31 - j39 \Omega$	$82 - j125 \Omega$	$21 + j17 \Omega$	$25 + j65 \Omega$

differential RCS of backscatter tags with two reflection states. For backscatter tags using more than two reflection states, we can modify the expressions to identify the worst-case differential RCS between any two reflection states, since this worst-case received power will determine the BER [15]. The differential RCS can thus be expressed as

$$\Delta\sigma = \frac{\lambda^2 G_{\text{ND}}^2}{4\pi} \min_{i,j \text{ for } i \neq j} |\Gamma_i^* - \Gamma_j^*|^2, \quad (10)$$

where  $\lambda$  is the free-space wavelength of the carrier wave,  $G_{\text{ND}}$  is the gain of the NeuroDisc antenna, and  $\Gamma_i^*$  and  $\Gamma_j^*$  are the reflection coefficients of the backscatter switch states. Considering RF impedances  $Z_i$  and  $Z_j$  with a resonant antenna impedance  $Z_{\text{ant}}$ , the reflection coefficients can be calculated:

$$\Gamma_{i,j}^* = \frac{Z_{\text{ant}}^* - Z_{i,j}}{Z_{\text{ant}} + Z_{i,j}}. \quad (11)$$

The backscatter power at the receiver is then

$$P_{\text{R}} = \frac{P_{\text{ND}}G_{\text{R}}\lambda^2}{(4\pi)^2 r_{\text{b}}^2} = \frac{P_{\text{T}}G_{\text{T}}\Delta\sigma G_{\text{R}}\lambda^2}{(4\pi)^3 r_{\text{t}}^2 r_{\text{b}}^2} \quad (12)$$

by combining equations (9) and (12) and noting that  $G_{\text{R}}$  is the gain of the receiver and  $r_{\text{b}}$  is the distance between the NeuroDisc and the receiver antennas. The link budget parameters for testing the NeuroDisc are shown in Table II.

#### V. EXPERIMENTAL RESULTS

Experiments were performed to validate the SSB backscatter communication uplink. Range experiments measured the effective packet error rate (PER) at different distances. A cabled experiment measured the SSB backscattered spectrum from the NeuroDisc. A data integrity test compared wirelessly uplinked data from the NeuroDisc to the original data to validate the NeuroDisc's complete signal chain.

##### A. Measured Backscattered Spectrum

The backscattered spectrum from the NeuroDisc was measured using the setup shown in Fig. 8(a). The NeuroDisc was configured to send BLE advertising packets like the one depicted in Fig. 4. An Agilent N5181A RF Signal Generator, an Agilent N9320B spectrum analyzer, and a MiniCircuits ZABDC20-252H-S+ coupler were used. The RF loads needed to create the constellation were determined based on methods presented in [23], with final component values chosen to be 0.6 nH, 6.8 nH, 3.3 pF, and 1.8 pF. The constellation shown in Fig. 8(b) was measured using an Agilent N5222A vector network analyzer. For the DSB modulation measurement, impedances Z0 and Z3 were used. The measurement revealed disparities in the relative angles and magnitudes of the reflection coefficients, likely due to impedance mismatches between the 50  $\Omega$  measurement equipment and the

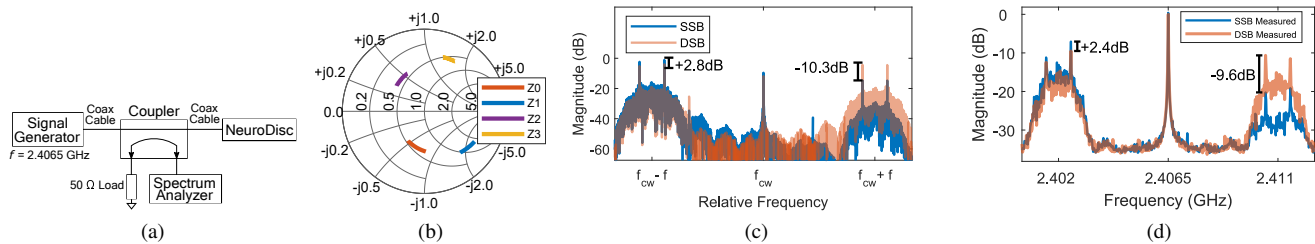


Fig. 8. (a) Experimental setup for measuring the NeuroDisc's backscattered spectrum, (b) Measured NeuroDisc symbol impedances, (c) Comparison of the simulated DSB and SSB spectra given the measured symbol impedances, (d) Comparison of the measured DSB and SSB spectra

NeuroDisc circuit board layout and component tolerances. While these mismatches reduced the sideband suppression ratio, the simulated and measured spectra in Fig. 8(c) and (d) successfully demonstrate suppression of the undesired sideband at 2.411 GHz while increasing the power of the desired sideband at 2.402 GHz. The measured sideband suppression was 10.0 dB, which shows good agreement with the 11.1 dB of sideband suppression in simulations generated from the measured symbol impedances.

### B. Modulator DC Power Consumption

To measure the modulator energy consumption, the RF switch was supplied with +3.3 V by a Keithley source-meter, and an Agilent 33500B Waveform Generator drove both control inputs of the switch at an average subcarrier rate of 4.75 MHz. The measured current was 60  $\mu$ A, resulting in a total power consumption (static + dynamic) at the backscatter modulator of 198  $\mu$ W. At a BLE data rate of 1 Mbps, this corresponds to an energy consumption of 198 pJ/bit.

### C. Range Testing

We measured the received signal strength from the NeuroDisc with respect to distance in the bistatic setup shown in Fig. 9. Measurements were performed in an empty parking garage that provided adequate space for range testing and isolation from other 2.4 GHz transmitters (e.g. WiFi and Bluetooth devices) that could interfere. Prior to testing, we surveyed the spectrum between 2.4-2.5 GHz to verify that no other transmitters were present. A calibrated Agilent N9320B Spectrum Analyzer was used to measure the received signal strength with a 10 kHz bandwidth. An Agilent N5181A RF Signal Generator and a MiniCircuits ZRL-3500+ RF amplifier were used to generate a carrier at 2.4065 GHz with a total RF output power of +20 dBm. The CW source, the spectrum analyzer, and the NeuroDisc used L-COM HG2402RDRSF antennas with gains of 2.2 dBi.

### D. Wireless Bio-Signal Uplink

To validate that biological signals could be captured and uplinked without distortion, we used the NeuroDisc to uplink low amplitude ( $<500$   $\mu$ V) pre-recorded neural data played back by an Agilent arbitrary waveform generator using the test setup shown in Fig. 10(a). Testing occurred in an ordinary office/lab environment. The same COTS BLE device from the range experiment was used to receive advertising packets

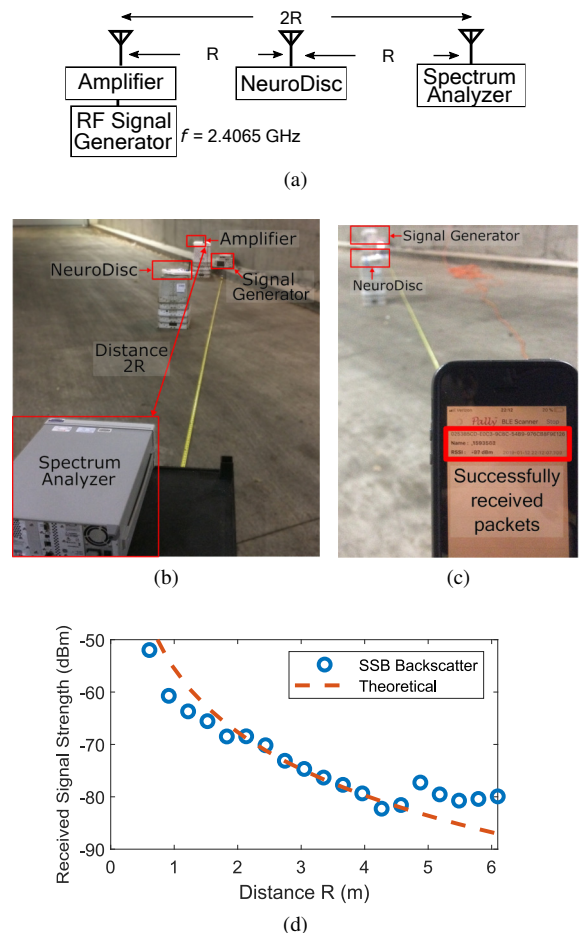


Fig. 9. Experimental setup for measuring the received signal strength vs. distance (a) Block diagram, (b) Photo, (c) BLE packets as received on a smartphone at a distance  $R = 6$  m, (d) Measured received signal strength vs. distance

from the NeuroDisc. An Agilent N5181A RF Signal Generator and a MiniCircuits ZRL-3500+ RF amplifier were used to generate a carrier at 2.4065 GHz with an RF output power of +20 dBm. Both the CW source and the nRF51822 used L-COM HG2402RDRSF antennas with a specified gain of 2.2 dBi. The NeuroDisc was configured to uplink packets at 500 Hz with one sensor sample per packet. The Intan chip was configured with a bandpass filter with a lower cutoff frequency of 0.1 Hz and an upper cutoff frequency of 200 Hz. Received packets were processed and plotted in MATLAB. The received biological data is plotted in Fig. 10(b) and shows that the original signal was successfully uplinked through the NeuroDisc and captured by a COTS Nordic Semiconductor

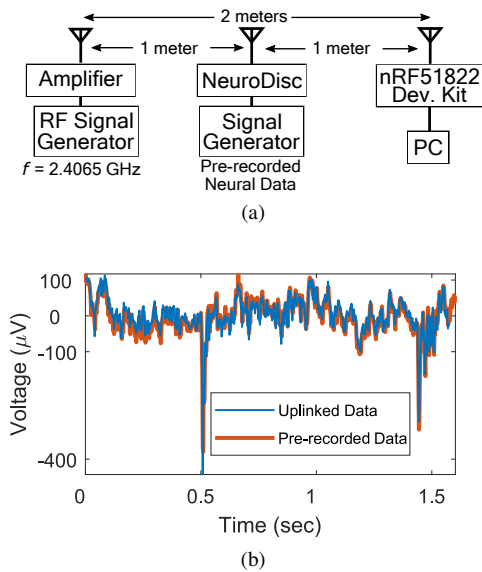


Fig. 10. (a) Setup for wirelessly uplinking pre-recorded neural test data, (b) Measured uplinked sensor data vs. re-recorded data

nRF51DK BLE evaluation board.

## VI. CONCLUSIONS & FUTURE WORK

In this work, we have demonstrated an energy efficient wireless uplink for the NeuroDisc brain-computer interface using single-sideband (SSB) Bluetooth Low Energy (BLE) backscatter communication. We presented a design methodology and simulations of SSB backscatter modulation using the phasing method and provided an analysis of how quadrature skew resulting from non-ideal impedance constellations results in reduced opposite-sideband suppression. These simulations were supported by measurements of the SSB backscattered spectrum in a cabled experiment and over-the-air (OTA) validation of the backscattered link budget in range measurements. End-to-end OTA measurements were then performed with the NeuroDisc sampling pre-recorded neural data, uplinking to an unmodified Nordic Semiconductor nRF51DK BLE receiver.

Future work includes refinement of the four impedances employed to fine-tune the achieved symbol impedances and thus improve the opposite-sideband suppression, as well as software development to implement additional portions of the Bluetooth protocol.

## ACKNOWLEDGMENT

The authors would like to thank the Fetz Lab of the University of Washington Dept. of Physiology & Biophysics for providing the pre-recorded neural data.

## REFERENCES

- [1] S. Zanos, A. G. Richardson, L. Shupe, F. P. Miles, and E. E. Fetz, "The Neurochip-2: an autonomous head-fixed computer for recording and stimulating in freely behaving monkeys," *IEEE Trans. Neural Syst. Rehabil. Eng.*, vol. 19, no. 4, pp. 427–435, 2011.
- [2] M. Yin, D. A. Borton, J. Aceros, W. R. Patterson, and A. V. Nurmikko, "A 100-channel hermetically sealed implantable device for chronic wireless neurosensing applications," *IEEE Trans. Biomed. Circuits Syst.*, vol. 7, no. 2, pp. 115–128, April 2013.

- [3] A. Jackson, J. Mavoori, and E. E. Fetz, "Correlations between the same motor cortex cells and arm muscles during a trained task, free behavior, and natural sleep in the Macaque monkey," *Physiology*, vol. 97, no. 1, pp. 360–374, Jan. 2007.
- [4] J. F. Ensworth and M. S. Reynolds, "Every smart phone is a backscatter reader: Modulated backscatter compatibility with Bluetooth 4.0 Low Energy (BLE) devices," in *Proc. 2015 IEEE Intl. Conf. RFID (RFID 15)*, April 2015, pp. 78–85.
- [5] X. Liu, M. Zhang, A. G. Richardson, T. H. Lucas, and J. V. der Spiegel, "Design of a closed-loop, bidirectional brain machine interface system with energy efficient neural feature extraction and PID control," *IEEE Trans. Biomed. Circuits Syst.*, vol. 11, no. 4, pp. 729–742, Aug 2017.
- [6] D. A. Schwarz *et al.*, "Chronic, wireless recordings of large-scale brain activity in freely moving rhesus monkeys," *Nature Methods*, vol. 11, no. 6, p. 670, 2014.
- [7] P. V. Nikitin, K. V. S. Rao, and R. D. Martinez, "Differential RCS of RFID tag," *Electronics Letters*, vol. 43, no. 8, pp. 431–432, 2007.
- [8] J. Rosenthal and M. S. Reynolds, "A 158 pJ/bit 1.0 Mbps Bluetooth Low Energy (BLE) compatible backscatter communication system for wireless sensing," in *Proc. 2019 IEEE Topical Conf. Wireless Sensors and Sensor Networks (WiSNet)*, Jan 2019, pp. 1–3.
- [9] V. Iyer, V. Talla, B. Kellogg, S. Gollakota, and J. Smith, "Inter-technology backscatter: Towards internet connectivity for implanted devices," in *Proceedings of the 2016 ACM SIGCOMM Conf.*, ser. SIGCOMM '16. New York, NY, USA: ACM, 2016, pp. 356–369.
- [10] V. Talla, M. Hesar, B. Kellogg, A. Najafi, J. R. Smith, and S. Gollakota, "LoRa backscatter: Enabling the vision of ubiquitous connectivity," *Proc. ACM Interact. Mob. Wearable Ubiquitous Technol.*, vol. 1, no. 3, pp. 105:1–105:24, Sep. 2017.
- [11] J. Kimionis and M. M. Tentzeris, "Pulse shaping: The missing piece of backscatter radio and RFID," *IEEE Trans. Microw. Theory Techn.*, vol. 64, no. 12, pp. 4774–4788, Dec 2016.
- [12] J. Rosenthal, E. Kampianakis, A. Sharma, and M. S. Reynolds, "A 6.25 Mbps, 12.4 pJ/bit DQPSK backscatter wireless uplink for the NeuroDisc brain-computer interface," in *Proc. 2018 IEEE Biomed. Circuits Syst. Conf. (BioCAS)*, Oct 2018, pp. 1–4.
- [13] D. E. Norgaard, "The phase-shift method of single-sideband signal generation," *Proceedings of the IRE*, vol. 44, no. 12, pp. 1718–1735, Dec 1956.
- [14] S. Gronemeyer and A. McBride, "MSK and Offset QPSK modulation," *IEEE Trans. Commun.*, vol. 24, no. 8, pp. 809–820, August 1976.
- [15] J. G. Proakis and M. Salehi, *Fundamentals of Communication Systems—2nd Ed.* Essex: Pearson, 2014.
- [16] Intan Technologies, LLC. RHS2000 series digital stimulator and amplifier chips. [Online]. Available: <http://intantech.com/>
- [17] Bluetooth Special Interest Group, *Bluetooth Core Specification v5.0*, Dec 2016.
- [18] J. F. Ensworth, "Ultra-low-power Bluetooth Low Energy (BLE) compatible backscatter communication and energy harvesting for battery-free wearable devices," Ph.D. dissertation, University of Washington, Dec. 2016.
- [19] D. M. Pozar, *Microwave Engineering—4th Ed.* Hoboken: John Wiley & Sons, Inc., 2012.
- [20] J. Kimionis, A. Bletsas, and J. N. Sahalos, "Increased range bistatic scatter radio," *IEEE Trans. Commun.*, vol. 62, no. 3, pp. 1091–1104, March 2014.
- [21] J. D. Griffin and G. D. Durgin, "Complete link budgets for backscatter-radio and RFID systems," *IEEE Antennas Propag. Mag.*, vol. 51, no. 2, pp. 11–25, April 2009.
- [22] J. F. Ensworth, A. T. Hoang, T. Q. Phu, and M. S. Reynolds, "Full-duplex Bluetooth Low Energy (BLE) compatible backscatter communication system for mobile devices," in *2017 IEEE Topical Conf. Wireless Sensors and Sensor Networks (WiSNet)*, Jan 2017, pp. 45–48.
- [23] S. J. Thomas and M. S. Reynolds, "A 96 Mbit/sec, 15.5 pJ/bit 16-QAM modulator for UHF backscatter communication," in *Proc. 2012 IEEE Intl. Conf. RFID (RFID 12)*, Apr. 2012, pp. 185–190.



**James Rosenthal** (S'16) received the B.S. degree in Electrical Engineering from the University of Minnesota, Minneapolis, MN, USA in 2013 and the M.S. degree in Electrical Engineering from the University of Washington, Seattle, WA, USA in 2018.

From 2013 to 2016 he was an electrical engineer at NASA Langley Research Center where he designed avionics systems for aerospace research projects. Since 2016 he has been a Ph.D. student in the Department of Electrical & Computer Engineering at University of Washington. His research is focused on the design of ultra-low power backscatter communication systems for biomedical applications.



**Matthew S. Reynolds** (S'01–M'02–SM'10) received the S.B., M.Eng., and Ph.D. degrees from the Massachusetts Institute of Technology (MIT), Cambridge, MA, USA, in 1998, 1999, and 2003, respectively.

He is currently an Associate Professor of Electrical and Computer Engineering at the University of Washington, Seattle, WA, USA. He is a co-founder of the RFID systems firm, ThingMagic Inc., the demand-side energy conservation technology firm Zensi, the home sensing company SNUPI Inc, and the millimeter wave imaging firm ThruWave Inc. His research interests include the physics of sensors and actuators, RF identification (RFID), microwave and millimeter wave imaging, and sensor signal processing.